

Thomas Ilzig, Daniel Schumacher, Michaela Wilhelm, Stefan Günther, Stefan Odenbach

Image data analysis of high resolution μ CT data for the characterization of pore orientation and pore space interconnectivity in freeze cast ceramics

Journal Article as: peer-reviewed accepted version (Postprint)

DOI of this document* (secondary publication): <https://doi.org/10.26092/elib/2514>

Publication date of this document: 15/11/2023

* for better findability or for reliable citation

Recommended Citation (primary publication/Version of Record) incl. DOI:

Thomas Ilzig, Daniel Schumacher, Michaela Wilhelm, Stefan Günther, Stefan Odenbach,
Image data analysis of high resolution μ CT data for the characterization of pore orientation and pore space
interconnectivity in freeze cast ceramics,
Materials Characterization, Volume 174, 2021, 110966, ISSN 1044-5803,
<https://doi.org/10.1016/j.matchar.2021.110966>

Please note that the version of this document may differ from the final published version (Version of Record/primary publication) in terms of copy-editing, pagination, publication date and DOI. Please cite the version that you actually used. Before citing, you are also advised to check the publisher's website for any subsequent corrections or retractions (see also <https://retractionwatch.com/>).

This document is made available under a Creative Commons licence.

The license information is available online: <https://creativecommons.org/licenses/by-nc-nd/4.0/>

Take down policy

If you believe that this document or any material on this site infringes copyright, please contact publizieren@suub.uni-bremen.de with full details and we will remove access to the material.

Image data analysis of high resolution μ CT data for the characterization of pore orientation and pore space interconnectivity in freeze cast ceramics

Thomas Ilzig^{a,*}, Daniel Schumacher^b, Michaela Wilhelm^b, Stefan Günther^a, Stefan Odenbach^a

^a Dresden University of Technology, Chair of Magneto-fluidynamics, Measuring and Automation Technology, George-Bähr-Straße 3, 01069 Dresden, Germany

^b University of Bremen, Advanced Ceramics, Am Biologischen Garten 2, IW3, 28359 Bremen, Germany

ARTICLE INFO

Keywords:

Pore space characterization
Pore space interconnectivity
Pore space orientation
High-resolution μ CT
Freeze-casting
Porous monoliths

ABSTRACT

Unidirectional and non-unidirectional freeze cast SiOC monoliths were characterized by means of digital image processing. For this purpose a novel method of pore segmentation in complex dendritic pore morphologies was developed. For the first time, the proposed method made it possible to perform an extensive geometrical and structural pore space characterization and analysis on single pore level. The orientation of the primary dendritic channels was obtained from high resolution μ CT images. Based on the mean directional vector distribution, the pore space was segmented. As a result, 95% (unidirectional) and 88% (non-unidirectional) of the original binary pore volume could be allocated to individual pores. The pore interconnectivity could be derived from this segmented pore space. It has been shown that the degree of interconnectivity between pores of the same orientation is higher than between pores of different orientation. This could be the reason for peculiar wicking behavior in non-unidirectional samples.

1. Introduction

Porous monolithic ceramics play an important role in scientific research as well as in engineering industry and medical technology. Typical applications are waste water treatment and filter applications [1], desalination plants [2] or tissue engineering [3]. But porous monoliths are also of interest in current research issues such as CO₂ storage [4], gas adsorption [5], catalytic processes [2] and novel high energetic accumulators [6, 7]. Beside interesting material properties such as chemical and thermal resistance, adjustable surface characteristics, comparatively low mass density, corrosion resistance and low thermal conductivity of porous ceramics, mass transport properties are of crucial interest for several applications. Decisive influencing factors for the mass transport in porous materials are the overall porosity, pore morphology, pore size distribution and pore interconnectivity.

Besides classical preparation techniques, the freeze-casting process is an important method to manufacture porous ceramic monoliths with a unique hierarchical pore structure. It is a segregation-induced templating process of a dispersed or dissolved second phase by a solidifying solvent [8, 9] [10]. The structure of freeze-cast ceramics is, depending on the manufacturing method and material composition, much more complex than that of a ceramic with spherical pores or ceramic sponges.

Using cyclohexane as solvent, ceramic monoliths with a dendritic pore structure can be obtained [11]: An elongated primary dendritic pore space which is interconnected by a multitude of secondary dendrites originating perpendicular out of the primary main channels. Variations of the freezing conditions, e.g. constant freezing temperature vs. constant freezing front velocity and non-unidirectional freezing vs. directional freezing lead to an inhomogeneous, non-aligned pore structure or to a homogeneous, fully aligned pore structure, respectively [12, 13, 14]. Moreover, in the case of non-unidirectional freeze cast ceramics, clusters of pores pointing in the same direction are formed. In their recent investigations, Schumacher and Zimnik [13] conducted capillary force-driven mass transport experiments (isothermal wicking) for morphologically different types of freeze cast ceramics. These experiments investigate the imbibition of a liquid into a porous structure with capillary forces being the driving force. Potential applications are propellant management devices in aerospace engineering [15, 16]. The results of these investigations however, revealed a peculiar wicking behavior for samples with non-unidirectional dendritic pore space. In contrast to the regular wicking behavior which is characterized by a constantly decreasing slope, the non-unidirectional sample showed a constant slope after an initial phase. Furthermore, the wicking speed was drastically reduced compared to the unidirectional sample. The

* Corresponding author.

E-mail address: thomas.ilzig@tu-dresden.de (T. Ilzig).

<https://doi.org/10.1016/j.matchar.2021.110966>

Received 18 August 2020; Received in revised form 12 January 2021; Accepted 12 February 2021

Available online 18 February 2021

authors attributed this behavior to a reduced interconnectivity between individual pores, but were not able to prove this hypothesis experimentally or by material characterization methods respectively. Against this background, the need for deeper analysis of complex pore structures through image analysis of CT data arose.

In general, the precise and reliable characterization of porous ceramics is essential to make these materials suitable for highly specialized applications. For this purpose, a number of experimental methods are available, which allow the characterization of decisive parameters. Features such as porosity, permeability, pore size and pore throat diameter are usually determined by mercury intrusion porosimetry (MIP) [17]. The specific surface of micro- and mesoporous materials can be measured by adsorption processes using the BET method [18]. Both are standard methods for the characterization of porous materials. Their major drawback is that they are both indirect methods which do not determine the quantities of interest by direct measurement [19]. Furthermore, for MIP measurements an assumption about the pore shape has to be made, which is not always possible a priori [20]. Another method frequently used in materials science is electron microscopy, which produces high-resolution images of material surfaces [21]. With this method, properties such as shape, position, size and interconnectivity of pores and pore networks can be assessed on a *random* basis. However, this form of imaging only provides two-dimensional information, the three-dimensional structure of complex samples cannot be assessed with these methods.

Modern imaging modalities such as X-ray computed microtomography (μ CT) allow the non-invasive acquisition of high-resolution CT images of almost arbitrary samples. Using suitable methods of digital image processing (DIP), it is possible to extract a variety of variables of interest from the image data, e. g. overall porosity and pore size and pore window size distribution. A special aspect is that these variables can be assigned to individual features in the sample. For example, in the case of a porous ceramic containing a volume of spherical pores, individual pores can be segmented using the watershed algorithm [22]. Reliable feature extraction methods such as binarization and segmentation algorithms build the basis for the structural characterization of complex porous structures. However, especially in the case of binary images, standard image processing methods such as the watershed algorithm tend to over-segmentation in the area of concave constrictions [22]. For this reason, this method fails when applied to complex dendritic porous structures. In order to overcome these deficiencies, different approaches have been proposed which fundamentally take into account the particularities of specific pore geometries. Due to the elongated basic shape of dendritic porous structures, the reduction of the pore volume to their medial axis is obvious.

Those reduction approaches have already been successfully applied to porous structures. Liebscher et al. evaluated the strut thickness of macroscopic open foams by investigation of the foams skeleton lines [23]. Besser et al. also used an approach based on the same method to characterize their porous structures [24]. Similar analyses is presented in [25,26]. However, in these examples the basic pore shape was spherical rather than elongated. Lin and Miller investigated filtration processes in filter cakes [19]. They derived models for the pore networks by skeletonization of the void phase from μ CT data. Their interest, however, lay in the morphology of the flow paths through the pore space. A segmentation approach to obtain individual pores was not pursued. Spanne et al. used morphological thinning to investigate the topology of open porous sandstones [27]. Sheppard et al. used a medial-axis transform to extract pore network topologies of different rock types [28]. The pore network thus formed was used as seeds for a watershed algorithm to segment and allocate individual pores. Although the pore structure in natural rocks is quite complex, the pore shape itself is often *convex*. A single pore is thus clearly demarcated from its adjacent neighbors, a feature which is not given in the case of dendritic porous topologies.

Fife et al. were the first who investigated μ CT data of aligned freeze-

cast titanium foams, including a 3D rendering of the dendritic pore structures [29]. Obmann et al. also investigated dendritic pore structures using μ CT data and obtained global characteristics such as porosity [30]. They also evaluated the individual strut thickness of the dendritic structures. Jeulin and Moreaud developed a gradient based method to evaluate the orientation of objects in 2D and 3D images in Fourier space [31]. Großberger et al. could use this approach to identify *clusters* of similarly oriented *lamellar* pores in freeze-cast alumina structures [32]. Deville et al. were able to study time-dependent crystal growth in a colloidal silica suspension using fast μ CT. The overall pore morphology in these samples resulted in lamellar dendritic structures [33]. Recent studies on freeze cast structures in solid solid-state batteries and Li/S cells [6, 7] also employed μ CT scans to obtain *overall* geometric data on pore space and pore morphology. Furthermore, in [6] a *two-dimensional* FFT-based image processing allowed a quantitative analysis of the interlayer spacing. To the best of our knowledge, however, in none of the presented studies a pore space segmentation on *single pore level* was addressed yet, especially not in *non-lamellar dendritic* structures – although the allocation of the pore space to individual pores is mandatory to evaluate features such as pore interconnectivity sufficiently.

Generally, the reduction of a complex geometry to a few resilient parameters and the modeling of the topology based on these parameters is the common feature of most of these studies. Typical characteristic values are the number and position of pores and pore throats or windows and the number of direct connections between several pores. The latter is a classical measure for the interconnectivity of porous structures [34, 35].

In contrast to these earlier works, however, the geometric complexity of the pore space of a dendritic freeze cast structure is significantly higher. This is in particular true in the case of non-unidirectional dendritic ceramics, due to a lack of clear demarcations between adjacent pores, a multitude of connections between different pores via primary *and* secondary dendrites and differently aligned pores in different clusters. Therefore, the aim of this work is to develop methods and strategies that provide a reliable pore segmentation in unidirectional and non-unidirectional freeze cast ceramic monoliths. Based on the segmented pore space, the evaluation of the main pore direction shall be carried out and a measure for the evaluation of pore interconnectivity shall be derived. Presenting a method that allows to elucidate sophisticated parameters and features in complex pore structures by image analysis of CT data is therefore the novelty of this work.

2. Materials and methods

2.1. Freeze-cast polymer derived ceramics

Porous ceramic monoliths were fabricated by solution-based freeze casting. A commercial methyl-polysiloxane (Silres® MK, Wacker Chemie AG, Germany) acted as preceramic polymer and (3-aminopropyl)triethoxysilane (APTES, abcr GmbH, Germany) served as cross-linking agent. Cyclohexane (CH, >99%, Sigma Aldrich Chemie GmbH, Germany) was used as solvent. No further treatment or purification of the raw materials was carried out.

The preparation of porous monolithic samples by solution-based freeze casting is shown in Fig. 1, whereas details of the process are described elsewhere [13, 14]. All mixing was carried out above the melting point of cyclohexane ($T_m(CH) = 6.5 \text{ }^\circ\text{C}$) at room temperature. Subsequent to the addition of MK and homogenization for 30 min under vigorous stirring, APTES was added at an amount of 1 mol%. The total solid loading mass set to 40 wt%, whereby the solid fraction was composed of preceramic polymer and cross-linking agent. After stirring for 3 min, degassing at 300 mbar for 30 s removed gas bubbles created during stirring. The solution was poured into a mold, which consists of a brass bottom and a transparent polycarbonate cylinder with an inner diameter of 40 mm and a height of 90 mm. The transparent mold allowed the observation of the freezing front and subsequently the

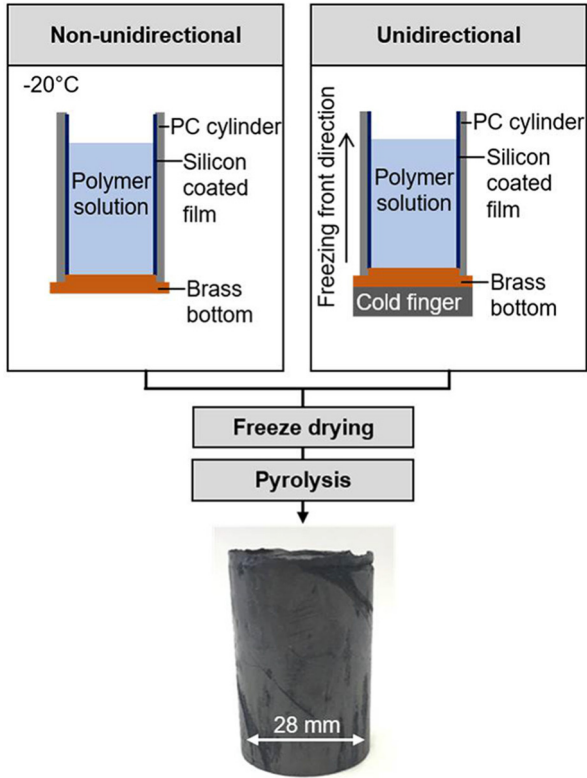


Fig. 1. Process scheme of the monolith preparation by solution-based freeze casting of polymeric solutions, left: non-unidirectional freezing at an ambient temperature of $-20\text{ }^{\circ}\text{C}$, right: unidirectional freezing on a cold finger at a constant freezing front velocity.

calculation of the freezing front velocity by analyzing video footage of the solidification process. A silicone coated polyethyleneterephthalat (PET) film (Hostaphan RN 30 2SLK, Mitsubishi Polyester Film GmbH, Germany) acted as a separation layer between solution and cylinder. The separation layer guaranteed easy demolding without damaging the frozen sample.

Basically, two different freezing conditions were applied to prepare two different kinds of samples: Non-unidirectional freezing conditions were achieved by transferring the mold to a freezer and freeze at an ambient temperature of $-20\text{ }^{\circ}\text{C}$ [13]. A freezing time of 72 h ensured sufficient cross-linking. In contrast, unidirectional freezing conditions required the controlled and directional freezing on a cold finger, which allows to adjust the temperature of the brass bottom in accordance to yield a constant freezing front velocity [14]. For this purpose, one end of the copper cold finger is immersed in liquid nitrogen, thus providing a sufficient temperature gradient. The other end of the cold finger is equipped with a resistance heater, which allows adequate temperature control during freezing and thus ensured a constant freezing front velocity. A thermocouple positioned at the center of the brass bottom detects the temperature at the interface between the brass bottom and sample. The temperature at the bottom of the mold was adapted to guarantee a constant freezing front velocity of $4\text{ }\mu\text{m/s}$. After complete freezing on the cold finger, the mold was transferred to a freezer at a temperature of $-20\text{ }^{\circ}\text{C}$ for 72 h to enable sufficient cross-linking.

Subsequently, the solvent was sublimated in a freeze dryer for 72 h at a shelf temperature of $-20\text{ }^{\circ}\text{C}$ and a pressure of 0.1 mbar. Lastly, the samples were pyrolyzed at $1000\text{ }^{\circ}\text{C}$ under flowing nitrogen with a heating rate of 2 K/min and a dwelling time of 4 h. The samples for the CT scan were taken from the center of the monoliths by cutting.

2.2. X-ray computed microtomography and basic image processing

2.2.1. X-ray computed microtomography

A commercial X-ray-microscope CT-scanner (Zeiss Xradia 520 Versa, Carl Zeiss Microscopy GmbH, Germany) was utilized to scan one unidirectional and one non-unidirectional freeze cast monolith of size $5 \times 5 \times 5\text{ mm}$ each. Acquisition parameters were set equal for both scans, except for the exposure time which had to be adjusted slightly for each sample. 3200 radiograms were taken from each sample which results into an angular increment of 0.1125° . Acceleration voltage was set to 80 kV and a cathode current was set to $88\text{ }\mu\text{A}$. Both scans were performed using a tungsten target. Geometrical magnification due to the cone beam was 3.5 and optical magnification was set to 4.0. Reconstruction was based on a FDK-algorithm [36] and the resulting voxel edge length of the reconstructed data was $1.92\text{ }\mu\text{m}$ due to a camera binning of 2. Due to Region-Of-Interest-tomography (ROI) [37] the reconstructed volume was $958 \times 958 \times 994\text{ vx}$ for the unidirectional sample and $968 \times 968 \times 1000\text{ vx}$ for the non-unidirectional sample. This results in a cylindrical volume of $\sim 1.8\text{ mm}$ in diameter for each dataset.

2.2.2. Basic image pre-processing

All image processing was performed using Python and its various open source library packages available [38] [39] [40]. From each reconstructed sample a representative sub volume of $500 \times 500 \times 500\text{ vx}$ was selected and cropped symmetrically around the central axes of each dataset (Fig. 2, a) and b)). The according grey level histograms reveal a clear bimodal grey level distribution. For this reason, a binary segmentation is first performed subsequently followed by a basic image pre-processing.

The aim of the pre-processing is to extract the medial axes of the primary dendrites, since their orientation is an essential feature of dendritic structures. The discrimination between primary and secondary dendrites can be obtained by thresholding the Euclidean distance transform (EDT) of the binary images. The pre-processing included:

1. median filtering for noise suppression and image smoothing,
2. image binarization by Otsu thresholding,
3. calculation of the EDT,
4. thresholding the EDT by an empirical threshold,
5. skeletonization of the discriminated EDT by a thinning algorithm,

and can be seen as an example in Fig. 3.

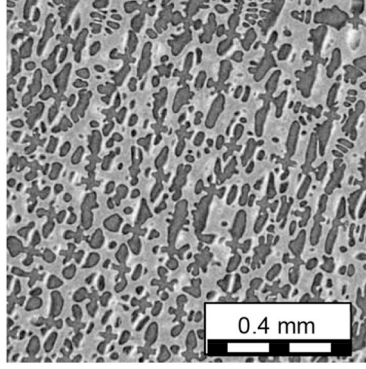
The skeleton line images were generated by morphological thinning. According to Maragos and Schafer the skeleton of a binary image conveys information about its size, orientation, and connectivity, features which are of interest for further analyses [41]. However, if the skeletonization is applied directly to the binary data of the pore volume, the secondary dendrites are also skeletonized. The result is a highly branched and complex network of skeleton lines which does not allow a distinction between primary and secondary dendrites. For this reason, skeletonization is applied to the previously discriminated distance transform, using

$$th_{EDT} = 0.5 \cdot \max(EDT) \quad (1)$$

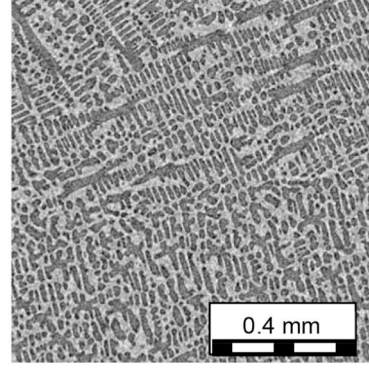
as an empirical threshold value. The thus discriminated EDT already shows the cylindrical primary dendritic structure and the subsequent skeletonization leads to a reduction to the medial axis of these cylinders (see Fig. 3 e).

2.3. Pore space orientation, segmentation and interconnectivity

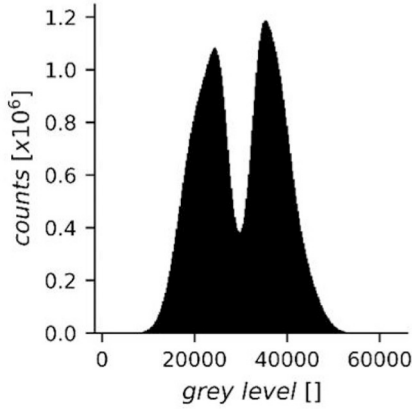
Subsequent to the basic image pre-processing a multistep approach is used to extract the desired features pore space orientation, segmented pore space and pore space interconnectivity. The pore space orientation refers essentially to the orientation of the medial axes of the primary



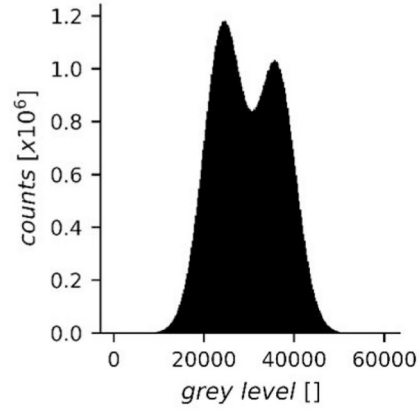
(a)



(b)



(c)



(d)

Fig. 2. X-ray μ CT scans of two polymer derived freeze cast ceramics. Two ROIs were chosen with a size of $500 \times 500 \times 500$ px each. (a) Unidirectional sample. (b) Non-unidirectional sample. (c) and (d) show the corresponding grey level histograms, which in both cases reveal a clear bimodal distribution. For reasons of comparability, REM images of both samples can be found in Fig. S 1 in the supplementary data.

dendrites. Once the orientation of the pores is obtained, a clustering of pores pointing in the same direction is possible. The orientation of the medial pore axes builds the basis for the subsequent pore space segmentation. The segmentation allows to allocate and distinguish between single pores. The further data analysis, such as the evaluation of the pore interconnectivity, can be carried out in depth on a single pore level.

2.3.1. Pore space orientation

The orientation of the pore space is based on the medial axes of the pores, obtained by thinning. In general, thinning algorithms are sensitive to boundary irregularities and noise in the image data [42]. This can lead to ambiguous skeletal lines, which are overdetermined and so-called simple points may remain on the medial axes which have to be removed [43] [44] [45]. This is required in order classify the axis points into ordinary strut points, endpoints and node points. For the detection of simple points, each voxel of the foreground and its $3 \times 3 \times 3$ environment is examined. If the test wise removal of the point in question does not change the topology within the environment, it is a simple point that can be deleted permanently.

After the removal of simple points, the medial axes appear unambiguous but, however, still have branches. In order to calculate the directional vectors of the medial axes, it is necessary to dissect these branched lines into unbranched segments. For this purpose, the axis points are classified according to the classification schemes presented in Eq. (2). Within a $3 \times 3 \times 3$ environment the pixel sum of the medial axis points is calculated. Since the skeleton lines are binary images, the pixel

sum reflects the number of contained foreground pixels. Accordingly:

$$\sum_{i=0}^2 \sum_{j=0}^2 \sum_{k=0}^2 I(x_i, y_j, z_k) = \begin{cases} 2, & \text{If the axis point is an endpoint,} \\ 3, & \text{If the axis point is an ordinary strut point,} \\ 4 \text{ or higher,} & \text{If the axis point is a node point.} \end{cases} \quad (2)$$

The classification of axis points is necessary to detect and subsequently delete the node points from the medial axes. After removal, each remaining axis segment (hereinafter referred to as strut) has exactly two unique endpoints. From the endpoint coordinates of each strut segment the directional vector can be derived by calculation of their Euclidean distance. This also yields the magnitude of each vector and allows the directional vectors to be expressed as unit vectors. Furthermore, very small strut fragments (≤ 2 px) are sorted out.

In order to classify the orientation of the struts, a cumulative frequency distribution in the form of a 2D histogram is derived from the set of single vectors (see Fig. 4). Here, the representation in spherical notation, i.e. by means of azimuthal and polar angle components is appropriate. The azimuthal component is divided into equidistant angular increments of 10° each. The polar component follows an arc cosine function to ensure that all area elements of the angular classes are of the same size and thus appear with the same probability in the histogram. Furthermore, the class entries are weighted with the vector magnitude and normalized with the number of entries per class.

The cumulative frequency distribution shows significant points of accumulation for the directional vectors belonging to the same cluster.

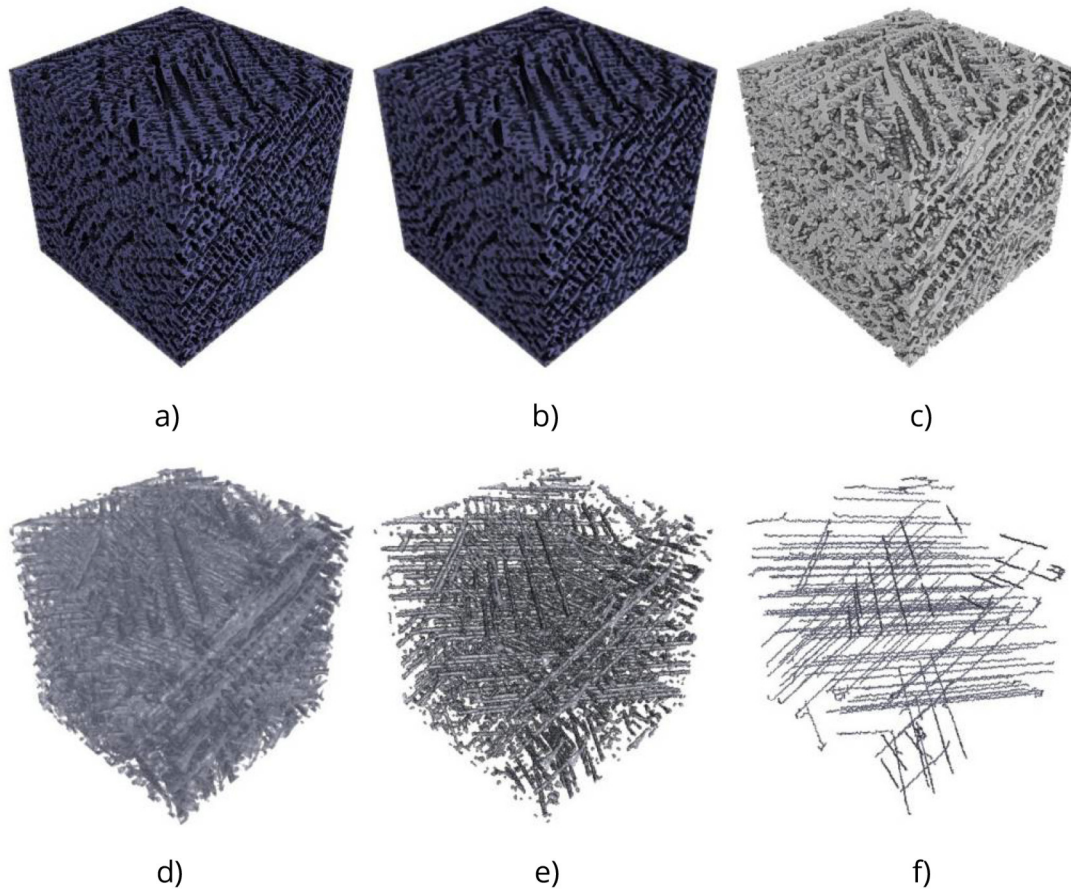


Fig. 3. Basic image processing steps (shown on a sub-sample of $200 \times 200 \times 200 \text{ px}^3$ for better visualization): a) grey level image, b) median filtered grey level image, c) thresholded binary image, d) Euclidean distance transform, e) thresholded EDT, f) skeletonized EDT yielding the medial axes of the primary dendritic structure.

Representative mean directional vectors can be formed for each cluster by averaging, whereby additionally an appropriate thresholding suppresses non-significant peaks. The assignment of the individual strut segments to a cluster is done by evaluating the scalar product between the individual direction vector and the mean class direction vector, for which a tolerance range of $\pm 15^\circ$ has been defined. This classification leads on the one hand to a significant data reduction. On the other hand, now defects in the strut network appear, since struts which cannot be assigned to any cluster are sorted out.

After the data reduction, the strut network is highly fragmented due to the removal of node points and non assigned struts. This means in particular that medial axes were separated which belong to a common continuous main axis of a pore. In the next process step, these fragments are reconnected, thus reconstructing the original pore medial axis. Since the node points usually do not contain more than three or four pixels, fragments belonging together are adjacent to each other. In order to detect adjacent struts, the end points of each strut are dilated spherically, using the value of the local EDT as dilation radius (Fig. S 2 in the supplementary data gives an example). In the case of closely adjacent segments, the spheres overlap in a certain transition area. Endpoints are reconnected with each other

- whose spheres share a common transition area,
- which belong to the same cluster, and
- which are aligned neighbors, or do not run parallel respectively.

To ensure that no parallel neighbors are reconnected, the directional vectors between the respective endpoints are calculated and compared

to the directional strut vectors. This way, continuous medial axes are generated whose orientation can be examined.

2.3.2. Pore space segmentation

In order to segment the original binary data into single pores, a watershed algorithm is utilized. The dendritic structures in the binary images show constrictions at the transition between primary and secondary dendrites. These constrictions would lead to an over-segmentation of the pore space. In order to avoid over-segmentation, a special profile image is generated from the medial axes which is then subjected to the watershed transformation. For this purpose, the medial axes are successively dilated. The dilation is carried out simultaneously for all struts and is locally terminated either if:

- a maximum amount of dilations is reached, determined by an average strut distance based on the Euclidean distance transform, or if
- two adjacent dilated strut regions begin to merge.

Furthermore, each dilation stage is multiplied by an increasing counter number. By doing so the value of dilation stages incrementally increases by 1 from the inside to the outside. Here the original medial axis has the value 1, the first dilation stage has the value 2 and so on. Fig. 5 a) shows the principle sketch for the generation of the dilation images and Fig. 5 b) gives an example from the investigated sample. The resulting images have an ideal height profile, with the strut segments lying at the lowest point and spots where adjacent regions merge form a ridge. This hill-valley profile is well suited for a subsequent watershed

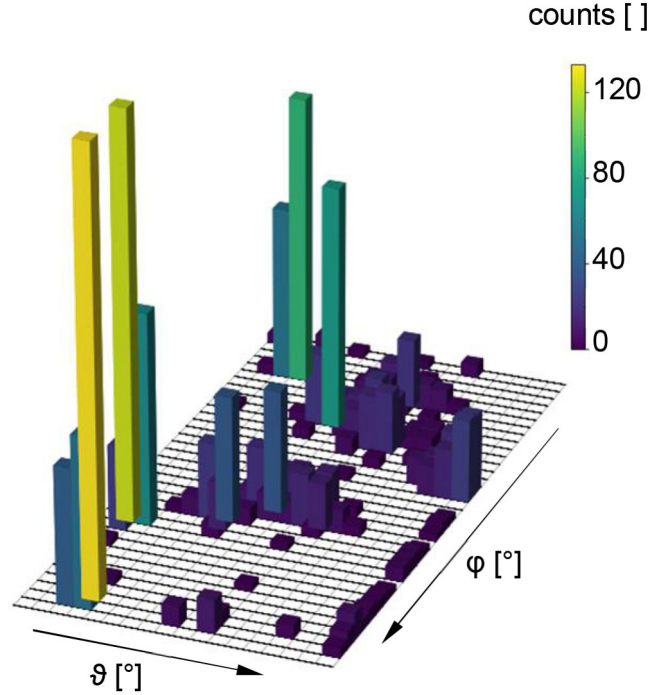


Fig. 4. Cumulative frequency distribution of the directional vectors (non-unidirectional sample). Significant points of accumulation show four peaks, representing four differently orientated clusters.

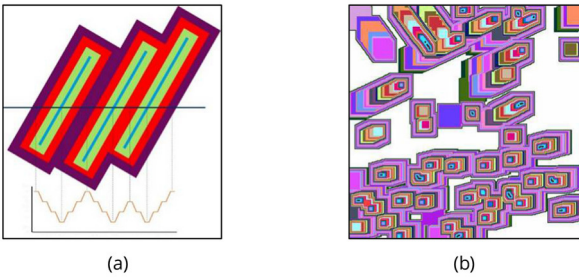


Fig. 5. (a) Principle sketch for the generation of dilation images. The connected and clustered struts are successively dilated. The voxel area of each dilation is multiplied by the count of previous dilation steps. Dilation stops whenever neighbored regions merge together or after a maximum amount of dilations is reached. In this way, images are created that have an ideal hill-valley profile for a subsequently following watershed algorithm (see plotted line profile below the sketch).

(b) Slice of the dilation image of the non-unidirectional sample, showing dilated struts from three different clusters. The color scheme indicates isolines of equal dilation numbers.

transformation. Here, a seeded watershed algorithm is used. Using the labeled struts as seeds, the resulting watershed transform is also labeled in the same way. The watershed image shows clear demarcations between adjacent regions. The segmented pore space is achieved by multiplication of the watershed transform with the original binary image of the pores.

2.3.3. Interconnectivity

The classical definition of the degree of interconnectivity of a pore network is given by Jones et al. [34]. Accordingly, the coordination number is the number of connections of a pore or node to other pores. A similar definition can be found in [35]. The mean coordination number is an important parameter for the description of pore networks and is

often characteristic for different types of porous materials [35].

In the case of dendritic freeze cast ceramics, a clear demarcation between neighbored pores is not given. The high degree of interconnection of adjacent pores mainly via secondary dendritic pore space makes it considerably more difficult to determine a clear boundary. For this reason, the definition of interconnectivity according to classical approaches is not applicable to the present problem. Therefore, the following definition for the characterization of interconnectivity in porous structures with dendritic pores is proposed:

$$C = \frac{A_{\text{trans}}}{A_{\text{surf}}} \quad (3)$$

This definition is applicable for single pores as well as for clusters of pores. Here, C denotes the interconnectivity, A_{surf} is the total surface area of a pore or a pore cluster and A_{trans} denotes the proportion of the surface that represents transition areas into adjacent pores or clusters. By -this definition, C is in between 0 and 1, whereby 0 represents no connections to other pores or clusters. However, in order to apply the above given definition of interconnectivity, a pore space segmentation is necessary, yielding individual assigned pore volumes.

In order to calculate the interconnectivity according to the above given definition, the surface area of the transition regions has to be determined. The principle is the same for single pores and pore clusters, thus only the procedure for single pores is described below. Due to the segmentation algorithm proposed in this work, adjacent pores which have transitions into each other touch without void space. This is due to the dilation of the strut structure, which terminates when adjacent areas merge. The quantitative determination of transition areas in a pore can therefore be done by separate dilation of adjacent pores. This requires a segmented pore space with individually labeled pores. The pore of interest remains unchanged, only the adjacent pores are dilated. Hereby, the dilated regions overlap the area of the not dilated pore. This overlap is the sought-after transition area of the non-dilated pore into its neighbors. If the pores are sorted by cluster, it is also possible to distinguish between cluster-internal transition areas and transitions into

other clusters (see Fig. 6).

3. Results and discussion

3.1. Pore structure and segmented pore space

3.1.1. General aspects

Discussion starts with some general aspects on pore size, pore and network structure as well as porosity Φ . The μ CT images in Fig. 2 show that the pore size in the unidirectional sample is larger than in the non-unidirectional sample. This is due to a limited freezing speed in the experimental setup for the fabrication of the unidirectional sample due to technical reasons. Therefore, fewer crystallization seeds are formed, which, however, grow longer after formation and form on average larger pores.

The general structure of a single pore is shown in Fig. 7 (a). In principle, the medial axis, the dendritic pore space and the transition areas can be seen. The main orientation of the pore is along its elongated main axis. The secondary dendritic pore space branches off perpendicular to the main longitudinal channel. The pores are mainly connected to each other via transitional regions in this secondary dendritic pore space.

If the same single pore is embedded in its immediate vicinity, the neighborhood relationships and the position of the individual pores to each other can be traced very well (Fig. 7 (b)). This pore ensemble was randomly selected from the unidirectional sample. The central pore is completely surrounded by adjacent pores. While this pore is almost symmetrical around its median axis, some of its neighbors show partly asymmetrical shapes. This is due to the position of the medial axes relative to each other, which serve as seeds for the successive dilatation. The figure also shows the current limits of the segmentation algorithm, because clear mis-segmentations are visible (e. g. the red pore space fragment on top right). These are due to erroneous remaining fragments in the strut network, which lead to an over-segmentation. The principle pore allocation, however, seems reasonable and comprehensible.

Open porosity Φ was determined from the binary image data and is defined as the ratio of volume of the void space to the bulk volume. The obtained values for the unidirectional and non-unidirectional sample are summarized in Table 1. For the purpose of comparison, open porosity Φ^* obtained by MIP measurements was included. MIP is an established standard method for the evaluation of open porosity in porous materials and therefore serves as reference method here. As can be seen in Table 1, the values obtained by digital image processing (DIP) differ from the values obtained by MIP. A major drawback of μ CT scans, is the limited

spatial resolution. Very small pore fractions near and below the resolution limit are not detected as well as details in surface roughness. These small-sized pore fractions might affect the accessible void space. For this reason, the values of the open porosity Φ obtained by DIP are assumed to be rather too low. Further reasons for miscalculations might be the size of the selected ROI and the choice of the threshold value for the binarization, although it is suspected that this will lead to rather minor deviations from the true value. The clear bimodal grey level distribution (see Fig. 2 (c)-(d)) enables a good binarizability of the pore volume. Nevertheless, due to the limited resolution of the μ CT scans, the true value of the porosity might be higher than the one obtained here.

3.1.2. Directional vector distribution

As expected, the vector distribution of the unidirectional sample only shows one peak, here at a polar angle of approx. 20° (Fig. 8 (a)). Fig. 8 (c) shows the strut elements corresponding to the determined directional vector distribution. The clustered strut image contains 123 distinguishable strut elements of varying length up to approx. 560 px, resulting in 108 reconstructed main channels. These 108 primary main axes were filtered from over 2300 strut elements which were originally contained in the unclustered strut image. The majority of these 2300 strut elements must therefore be assigned to the secondary dendritic pore space.

In contrast, Fig. 8 (b) shows multiple peaks in the mean directional vector distribution of the non-unidirectional sample. In total four peaks of four different directional clusters are visible. The different size of the clusters, referred to the number of strut segments contained, is due to boundary effects of the chosen ROI. The length of the contained strut elements varies up to approx. 520 px and is therefore in the same order of magnitude as for the unidirectional sample. This is clearly an effect of the chosen ROI size, which shows only a section of a larger volume.

From originally over 4900 strut elements, the clustered strut image presented in Fig. 8 (d) still contains 430 distinguishable entities. Thus, even in the case of the non-unidirectional sample, a large part of the objects contained after thinning and removal of the node points, is attributable to the secondary dendritic pore space. The orientation of the mean direction vectors covers almost the whole azimuthal angular range of the hemisphere but a small polar angular range which is in between approx. 15° and 55° . Principally, the spatial distribution of the clusters does not allow any conclusion about possible directional preferences of crystal growth during phase separation and thus, the directional vectors are assumed to be randomly distributed.

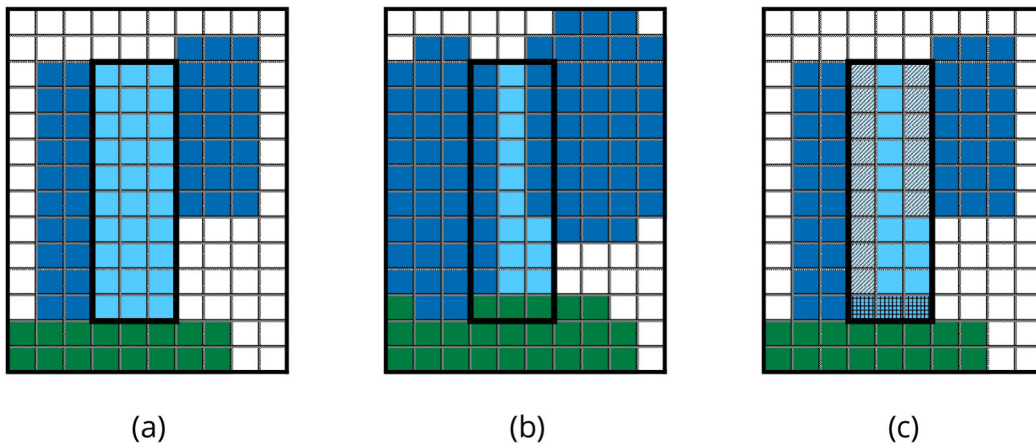


Fig. 6. Principle sketch for the detection of transition areas. (a) Four pores of two clusters (blue and green) are adjacent to each other. (b) Dilatation of the adjacent pores into the light-blue pore. (c) Transition areas of the light-blue pore (crosshatched boxes). It has internal transitions into the dark-blue pores and external transition into the green pore. (For interpretation of the references to color in this figure legend, the reader is referred to the web version of this article.)

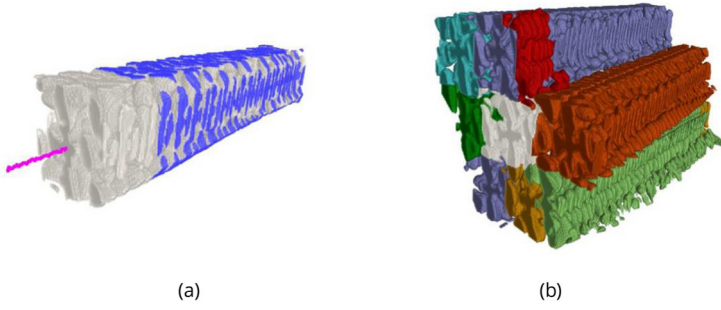


Fig. 7. (a) General structure of a typical segmented single pore. The medial axis (purple), the secondary dendritic pore space (white) and the transition area into adjacent pores (blue) are visualized. For reasons of visualization the transitional regions and secondary dendrites are shown graded and stripped back. (b) The same (central) pore embedded in its immediate vicinity. The pore ensemble was taken from the unidirectional sample. Some of the pores have a strong asymmetrical shape, what can be addressed to the relative position of the medial axes to each other. Furthermore, pore space mis-segmentations are clearly visible (red pore fragment on top right), which are due to erroneous remaining strut fragments in the strut network. (For interpretation of the references to color in this figure legend, the reader is referred to the web version of this article.)

Table 1
Summary of the main results of the material characterization derived from μ CT-measurements.

	Unidirectional sample	Non-unidirectional sample				
Porosity φ []	0.478	0.522				
Porosity φ^* []	0.61	0.58				
Cluster number	–	1	2	3	4	Total
Number of pores N []	108	144	123	81	82	430
Mean surface to volume ratio [μm^{-1}]	0.192	0.241	0.241	0.247	0.250	0.246
Total interconnectivity C_{total} []	0.165	0.199	0.212	0.226	0.185	0,205
Intern interconnectivity C_{intern} []	–	0.169	0.177	0.166	0.120	–
Extern interconnectivity C_{extern} []	–	0,030	0.035	0.059	0.066	–

* Obtained by MIP.

3.1.3. Segmented pore space

The complete segmented pore space of the unidirectional and the non-unidirectional sample are presented in Fig. 9. The single pores are labeled individually and displayed in different colors.

In the case of the unidirectional sample, the same spatial orientation of the pores is clearly visible. Furthermore, the dendritic shape of the individual pores can be easily observed. The volume segmented in this way covers about 95% of the original binary volume. However, this does not mean that 95% of the binary volume has been correctly segmented. The quality of the segmentation depends primarily on the quality of the reconstructed struts. If fragmented objects remain in the strut image after the reconstruction of the strut lines, i.e. objects that belong to a common main channel line but are not connected, the pore volume is also fragmented at this point. Nevertheless, the fact that such a high percentage was detected in the segmented pore image indicates that only few gross defects remained in the strut image. It should be mentioned that the choice of the structural element during successive dilatation of the struts also has a great influence on the result of the segmentation. Since the orientation of the secondary dendritic pore space relative to the main channels is not known a priori and can also vary, a cube-shaped structural element was used in this case. If a cross-shaped structural element was chosen, only a significantly lower percentage of the binary volume would be covered by the segmentation algorithm.

In the case of the non-unidirectional sample, pores can be detected which are aligned in the same direction and thus belong to the same cluster. The dendritic pore structure is also clearly visible here. The arrangement of the pores seems rather chaotic at first, but in comparison with the strut image in Fig. 8 (b) it can be well understood, at least for the pores in edge regions. In total, about 88% of the original binary volume was allocated to the segmented pore space. The lower percentage compared to the unidirectional sample indicates more defects in the connected strut image. The main reason for these defects is probably the more complex structure of the sample itself and the comparatively smaller pores at the same spatial resolution of the μ CT data. Therefore, the probability of fragmented main channels is higher, because the length of the individual strut elements is shorter on average and the scattering of their directional vectors can therefore be higher. As a

result, the probability of unassignable strut elements is also higher and defects in the strut network are more likely.

Since the discussed segmentation approach is based on the evaluation of the medial axes of elongated objects, the algorithm is not limited to dendritic pore spaces. One of the most beneficial aspects is, that it can be easily adapted to other complex pore morphologies e. g. prismatic pore shapes.

3.2. Interconnectivity

The evaluation of the interconnectivity is first performed comparatively for the unidirectional and the non-unidirectional sample.

Fig. 10 shows the interconnectivity C over the surface-to-volume ratio for both samples on a single pore level. The respective frequency distributions are additionally plotted. Note that the histograms are not based on a normal distribution, which is illustrated by their kernel density estimations (KDE). The surface-to-volume ratio is well suited for the estimation of the mean pore size. As expected, this ratio is smaller for the larger pores of the unidirectional sample. The frequency distributions or KDEs of the surface-to-volume ratios allow a clear distinction between the unidirectional and non-unidirectional sample. In contrast, this clear distinction between both samples based on the distributions of the interconnectivity is not possible. This shows that the interconnectivity is very similar for both samples. Despite a certain scattering, there is a concentration of values in a certain range. Nevertheless, the scatter of the values for the non-unidirectional sample is significantly higher and the KDEs are correspondingly flatter and wider. The reason for the higher scatter is, as stated in the evaluation of the pore segmentation, the higher complexity of the sample itself and the smaller pore sizes on average.

In the case of the non-unidirectional sample, the evaluation of the interconnectivity can be differentiated for the different clusters. Principally connections between the clusters can occur via primary and secondary dendrites, whereas connections of the pores within a cluster are only possible via the latter. The proposed algorithm is not yet able to distinguish between primary and secondary interconnection, but between internal and external interconnection, or transitions within a cluster and between different clusters, respectively. This is illustrated in

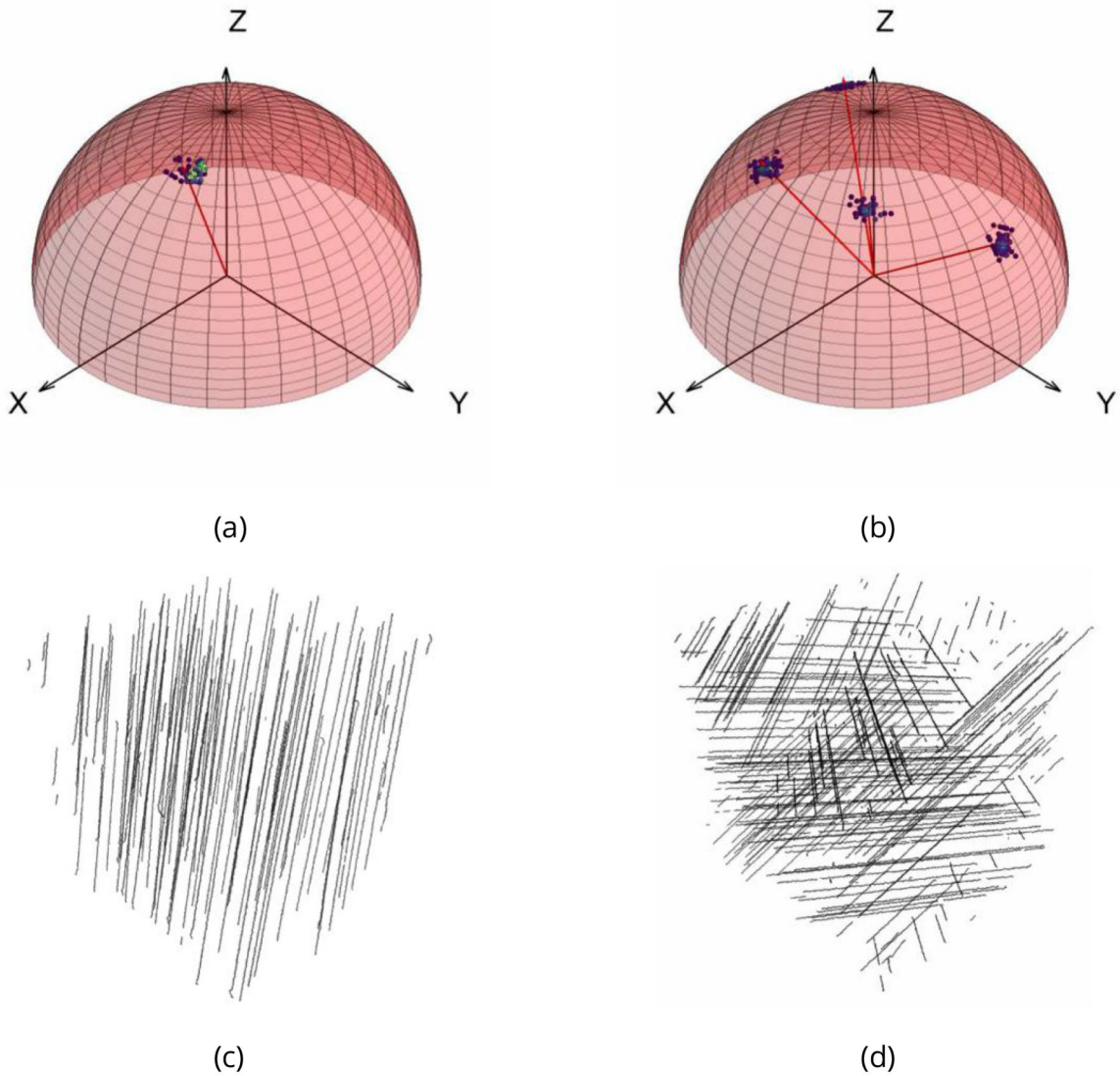


Fig. 8. Mean direction vector distribution, plotted as unit vectors on a hemisphere. (a) Vector distribution of the unidirectional sample. The main direction is aligned with the x-axis. (b) Vector distribution of the non-unidirectional sample. Each cluster point indicates the main direction of aligned primary dendrite structures. In total, four different clusters are visible. (c) and (d) Clustered strut images of the unidirectional and the non-unidirectional sample, respectively.

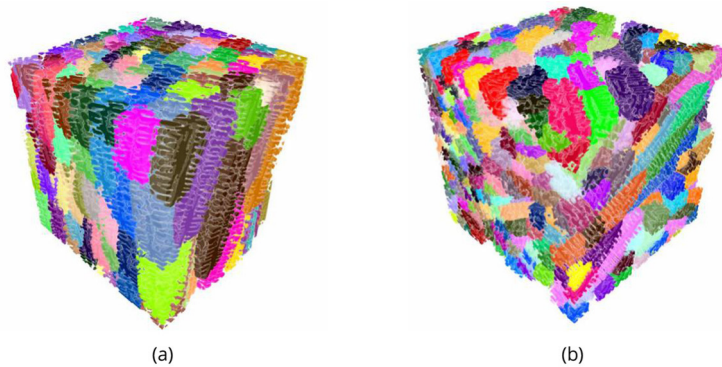


Fig. 9. Segmented and labeled pore space. Each segmented pore has its own identifier (label), which is represented by an individual color. (a) Segmented pore space of the unidirectional sample. All pores point in the same direction, as expected from the directional vector distribution. (b) Segmented pore space of the non-unidirectional sample. The pore orientation shows several clusters of pores, pointing in the same direction.

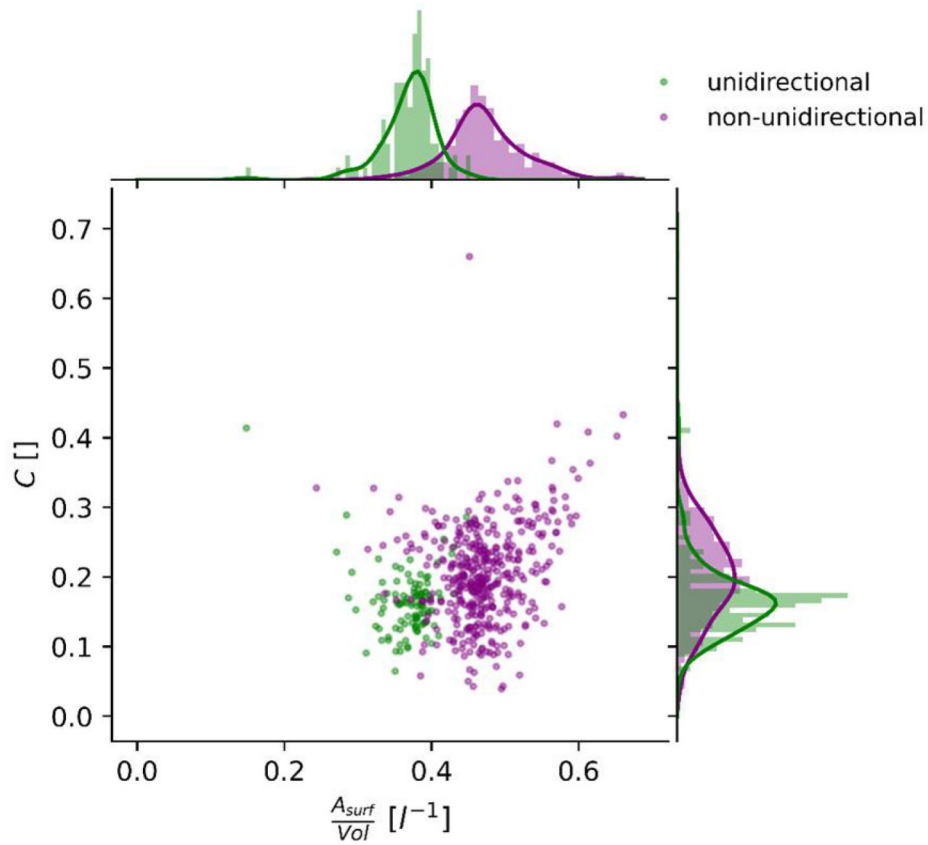


Fig. 10. Interconnectivity C over Surface-to-Volume ratio on a single pore level for the unidirectional and the non-unidirectional sample, including the respective frequency distributions and KDEs.

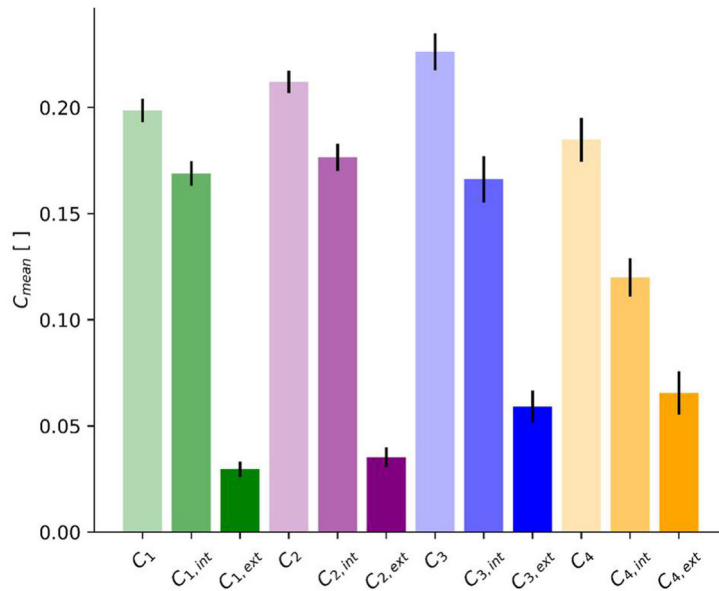


Fig. 11. Mean values of the total, internal and external interconnectivity for the four clusters.

Fig. 11, which shows the mean values of total (C_{tot}), internal (C_{intern}) and external (C_{extern}) interconnectivity for the different clusters. In the case of a single pore, C_{tot} is equal to the sum of C_{intern} and C_{extern} . However,

due to the representation as a mean value over an ensemble of pores, this relationship is no longer valid for the shown diagram. Furthermore, since the data is not normally distributed, the mean values and standard

errors of each bar were determined by bootstrapping the data [46].

The diagram shows that the mean value for each cluster is around 0.2. Two things are particularly striking:

- 1) The external interconnectivity for clusters 3 and 4 is about twice as high as for clusters 1 and 2, and
- 2) the internal interconnectivity for each cluster is significantly higher than the external.

The reason for 1) is primarily the size and the shape of the clusters, which are mainly determined by the size and position of the ROI. Clusters 1 and 2 consist of significantly more pores than clusters 3 and 4, which is why there are more pores in the first two clusters that only have cluster-internal connections to other pores. Furthermore, clusters 3 and 4 have a more contorted or angled shape overall, while clusters 1 and 2 are more cuboid. This leads to more transition areas into adjacent clusters. It can be expected that the shown differences in C_{extern} would disappear with increasing ROI size.

Although 2) was expectable this observation allows to draw some interesting conclusions on the findings of recent studies on isothermal wicking of Schumacher and Zimnik [13]. As described in section 1 the observed wicking behavior of samples with non-unidirectional dendritic pore morphology could not be mapped with the existing model ('peculiar wicking'). It was suspected that the real pore topology and the presence of a primary and a secondary dendritic pore space led to the reported unpredictable behavior. Both are parameters that are not found in the model used to describe wicking. In fact, the basic assumption of the model, a bundle of straight, not connected capillaries, is not even roughly fulfilled for the non-unidirectional sample, while it is valid for the unidirectional sample in good approximation. The significantly reduced external interconnectivity compared to the internal interconnectivity supports the statement that the peculiar wicking behavior is caused by a lack of connections between pores of different clusters. The further expressed assumption that the differences in wicking between unidirectional and non-unidirectional dendritic ceramics could be due to the fact, that the mass flow is mainly through the primary dendritic pores can neither be proved nor disproved by the present study. As already mentioned, this would require the distinction between primary and secondary transition.

4. Conclusions

The segmentation of complex porous structures is a non-trivial problem of general interest in material science. In this work, we presented an algorithm for the segmentation and characterization of complex dendritic porous structures, based on high resolution μ CT images. For this purpose, porous polymer-derived ceramic monoliths (SiOC) were prepared by solution based-freeze casting. Samples with isotropic unidirectional and anisotropic non-unidirectional pore structure were prepared and scanned by an X-ray-microscope CT-scanner. The medial axes of the pre-processed image data were obtained by thinning and strut segments with unique start and end points were extracted. From this information a directional distribution of the strut segments could be obtained and a clusterwise assignment of individual segments by direction was performed. From the clustered strut segments, continuous main channel axes were reconstructed, which after a successive dilation formed the basis for a seeded watershed algorithm. This made it possible to separate individual pores from each other and thus segment the pore space. From the surface of the individual pores, the proportion that forms transition areas into other pores was determined. A measure for the interconnectivity of each individual pore could be calculated from these transition areas. The general approach of the proposed segmentation method is based on the evaluation of the medial axes of elongated objects. Therefore, the algorithm is not limited to dendritic pore spaces, but can be applied to other complex pore morphologies e. g. prismatic pore shapes.

The directional vectors of the struts showed the expected distribution for both samples. A single significant peak for the primary dendritic pore space in the unidirectional sample and four significant clusters in the non-unidirectional sample. The spatial distribution of the clusters does not allow any conclusion about the directional preferences of crystal growth during phase separation, so that it can be assumed that the directional distribution is randomly distributed.

The pore space segmentation shows good results for both samples in general. The evaluated image data enables to comprehend the dendritic pore structure and their position relative to each other. However, the percentage of allocated pore volume to the original binary volume is higher for the unidirectional sample. The reason could be the more complex structure of the non-unidirectional sample in general, and its smaller pore size in particular. Unallocated pore volume is mainly attributed to remaining fragmentation of the struts, which is also the main reason for misallocations.

The evaluation of the interconnectivity showed similar results for both samples. On average, the total interconnectivity for the pores of both samples was about 0.2. As both samples have the same pore morphology, this finding is plausible. In the case of the non-unidirectional sample, it was possible to distinguish between internal interconnectivity, i.e. transition regions within a cluster, and external interconnectivity, i.e. transition regions between pores of different clusters. For external interconnectivity, differences were found between the pores from the larger clusters 1 and 2 and those from the smaller clusters 3 and 4. The main reason for this is probably the different number of pores and especially the contorted shape of the smaller clusters, so that C_{extern} was twice as large as in the other clusters. This effect is attributed to the size and position of the chosen ROI. Common to all four clusters was that their internal interconnectivity was significantly higher than their external interconnectivity. Although this finding is not surprising, it supports corresponding hypotheses concerning peculiar wicking behavior from previous work.

Disclosure statement

No potential conflict of interest was reported by the authors.

Declaration of Competing Interest

The authors declare that they have no known competing financial interests or personal relationships that could have appeared to influence the work reported in this paper.

Acknowledgement

This work was supported by German Research Foundation (DFG) within the Research Training Group GRK 1860 'Micro-, meso- and macroporous nonmetallic Materials: Fundamentals and Applications' (MIMENIMA).

The authors further wish to thank 'MAPEX: Center for Materials and Processes' at the university of Bremen as well as Oliver Focke and Jürgen Horvath for conducting the μ CT-measurements.

Moreover, Thomas Ilzig wants to thank Lukas Selzer for fruitful discussions and first aid in pythonic programming.

Appendix A. Supplementary data

Supplementary data to this article can be found online at <https://doi.org/10.1016/j.matchar.2021.110966>.

References

- [1] T. Fukasawa, M. Ando, T. Ohji, Filtering properties of porous ceramics with unidirectionally aligned pores, *J. Ceram. Soc. Jpn.* 110 (1283) (2002) 627–637.

- [2] C. Gaudillere, J. Manuel Serra, Freeze-casting: fabrication of highly porous and hierarchical ceramic supports for energy applications, *Boletín De La Sociedad Espanola De Ceramica Y Vidrio* 55 (2) (03 2016) 45–54.
- [3] J. Woodard, A. Hilldore, S.K. Lan, C.J. Park, A.W. Morgan, J.A.C. Eurell, S.G. Clark, M. Wheeler, R. Jamison, A.J. Wagoner Johnson, The mechanical properties and osteoconductivity of hydroxyapatite bone scaffolds with multi-scale porosity, *Biomaterials* 28 (1) (01 2007) 45–54.
- [4] N. MacDowel, N. Florin, A. Buchard, J. Hallett, A. Galindo, G. Jackson, C. S. Adjiman, C. Williams, N. Shah, P. Fennell, An overview of CO₂ capture technologies, *Energy Environ. Sci.* 3 (11) (2010) 1645.
- [5] S. Kenarsari, D. Yang, G. Jiang, S. Zhang, J. Wang, A. Russel, Q. Wei, M. Fan, Review of recent advances in carbon dioxide separation and capture, *RSC Adv.* 3 (45) (2013) 22739.
- [6] E. Yi, H. Shen, Y. Sung, J. Kou, K. Chen, D.Y. Parkinson, M.M. Doeff, E.J. Cairns, Three-dimensionally aligned sulfur electrodes by directional freeze tape casting, *Nano Lett.* 19 (7) (10 07 2019) 4731–4737.
- [7] E. Yi, H. Shen, S. Heywood, J. Alvarado, D.Y. Parkinson, G. Chen, S.W. Sofie, M. M. Doeff, All-solid-state batteries using rationally designed garnet electrolyte frameworks, *ACS Appl. Energy Mater.* 3 (1) (27 01 2020) 170–175.
- [8] S. Deville, *Freezing Colloids: Observations, Principles, Control, and Use*, Springer International Publishing, 2017.
- [9] S. Deville, Freeze-casting of porous ceramics: a review of current achievements and issues, *Adv. Eng. Mater.* 10 (3) (2008) 155–169.
- [10] S. Deville, Ice-templating, freeze casting: beyond materials processing, *J. Mater. Res.* 28 (17) (09 2013) 2202–2219.
- [11] M. Navroji, S. Miller, P. Colombo, K. Faber, Directionally aligned macroporous SiOC via freeze casting of preceramic polymers, *J. Eur. Ceram. Soc.* 8 (35) (2015) 2225–2232.
- [12] S. Deville, E. Saiz, R.K. Nalla, A.P. Tomsia, Freezing as a path to build complex composites, *Science* 311 (5760) (27 01 2006) 515–518.
- [13] D. Schumacher, D. Zimnik, M. Wilhelm, M. Dreyer, K. Rezwan, Solution based freeze cast polymer derived ceramics for isothermal wicking - relationship between pore structure and imbibition, *Sci. Technol. Adv. Mater.* 20 ((1) (31 12 2019) 1207–1221.
- [14] D. Schumacher, P. da Rosa Braun, M. Wilhelm, M. Dreyer, K. Rezwan, Unidirectional solution-based freeze cast polymer-derived ceramics: influence of freezing conditions and templating solvent on capillary transport in isothermal wicking, *J. Mater. Sci.* 55 (2020) 4157–4169.
- [15] D. Jaekle, Propellant management device conceptual design and analysis - Sponges, in: *29th Joint Propulsion Conference and Exhibit*, Monterey, CA, U.S.A., 1993.
- [16] M. Wollen, F. Merino, J. Schuster, C. Newton, *Cryogenic Propellant Management Device*, NASA Scientific and Technical Information, Cleveland Ohio, 2010.
- [17] A.B. Abell, K.I. Willis, D.A. Lange, Mercury intrusion porosimetry and image analysis of cement-based materials, *J. Colloid Interface Sci.* 211 (1) (03 1999) 39–44.
- [18] S. Brunauer, P.H. Emmet, E. Teller, Adsorption of gases in multimolecular layers, *J. Am. Ceram. Soc.* 60 (2) (02 02 1938) 309–319.
- [19] C.L. Lin, J.D. Miller, Pore structure and network analysis of filter cake, *Chem. Eng. J.* 80 (1) (01 12 2000) 221–231.
- [20] D. Lange, H. Jennings, S. Shah, Image analysis techniques for characterization of pore structure of cement-based materials, *Cem. Concr. Res.* 24 (5) (01 01 1994) 841–853.
- [21] U. Valdre, *Electron Microscopy in Material Science*, Academic Press, London, New York, 1971.
- [22] S. Beucher, F. Meyer, The morphological approach to segmentation: the watershed transformation, in: *Mathematical Morphology in Image Processing*, Marcel Dekker Inc., New York, 1993, pp. 433–480.
- [23] A. Liebscher, C. Redenbach, Statistical analysis of the local strut thickness of open cell foams, *Image Anal. Stereol.* 32 (1) (19 03 2013) 1–12.
- [24] B. Besser, H. Tajiri, G. Mikolajczyk, J. Möllmer, J. Schumacher, S. Odenbach, R. Gläser, S. Kroll, K. Rezwan, Hierarchical porous zeolite structures for pressure swing adsorption applications, *ACS Appl. Mater. Interfaces* 8 (5) (10 02 2016) 3277–3286.
- [25] K. Schelm, T. Fey, K. Dammler, U. Betke, M. Scheffler, Hierarchical-porous ceramic foams by a combination of replica and freeze technique, *Adv. Eng. Mater.* 21 (6) (2019) 1801362.
- [26] T. Fey, B. Zierath, P. Greil, M. Ptoczek, Microstructural, mechanical and thermal characterization of alumina gel-cast foams manufactured with the use of agarose as gelling agent, *J. Porous. Mater.* 5 (22) (01 10 2015) 1305–1312.
- [27] P. Spanne, J.F. Thovert, C.J. Jacquin, W.B. Lindquist, K.W. Jones, P.M. Adler, Synchrotron computed microtomography of porous media: topology and transports, *Phys. Rev. Lett.* 73 (14) (03 10 1994) 2001–2004.
- [28] A.P. Sheppard, R.M. Sok, H. Averdunk, Improved pore network extraction methods, in: *International Symposium of the Society of Core Analysts*, Toronto, 2005.
- [29] J. Fife, J. Li, D. Dunand, P. Voorhees, Morphological analysis of pores in directionally freeze-cast titanium foams, *J. Mater. Res.* 24 (01) (2009) 117–124.
- [30] R. Obmann, S. Schörpf, C. Gorsche, R. Liska, T. Fey, T. Konegger, Porous polysilazane-derived ceramic structures generated through photopolymerization-assisted solidification templating, *J. Eur. Ceram. Soc.* 39 (4) (01 04 2019) 838–845.
- [31] D. Jeulin, M. Moreaud, Segmentation of 2D and 3D textures from estimates of the local orientation, *Image Anal. Stereol.* 27 (3) (03 05 2011) 183–192.
- [32] S. Großberger, T. Fey, G. Lee, Vacuum-induced surface freezing to produce monoliths of aligned porous alumina, *Materials* 9 (12) (05 12 2016).
- [33] S. Deville, J. Adrien, E. Maire, M. Scheel, M.D. Michiel, Time-lapse, three-dimensional in situ imaging of ice crystal growth in a colloidal silica suspension, *Acta Mater.* 61 (6) (2013) 2077–2086.
- [34] A. Jones, C. Arns, D. Huttmacher, B.K. Milthorpe, A.P. Sheppard, M.A. Knackste, The correlation of pore morphology, interconnectivity and physical properties of 3D ceramic scaffolds with bone ingrowth, *Biomaterials* 30 (7) (01 03 2009) 1440–1451.
- [35] K.C. Khilar, H.S. Fogler, *Migrations of Fines in Porous Media Bd. 12*, Kluwer Academic Publishers, Dordrecht, Boston, London, 1998.
- [36] I.A. Feldkamp, I.C. Davis, J.W. Kress, Practical cone-beam algorithm, *J. Opt. Soc. Am. A* 1 (6) (01 06 1984) 612.
- [37] S. Azevedo, P. Rizo, P. Grangeat, Region-of-interest cone-beam computed tomography, Lawrence Livermore National Laboratory, Livermore, CA, USA, 1995.
- [38] G. van Rossum, F.L. Drake, *Python 3 Reference Manual: (Python Documentation Manual Part 2)*, CreateSpace, Scotts Valley, CA, USA, 2009.
- [39] P. Virtanen, R. Gommers, et al., SciPy 1.0—fundamental algorithms for scientific computing in python, *Nat. Methods* 17 (3) (03 2020) 261–272.
- [40] S.V.D. Walt, J.L. Schönberger, J. Nunez-Iglesias, F. Boulogne, J.D. Warner, N. Yager, E. Gouillart, T. Yu, scikit-image: image processing in Python, *PeerJ* 2 (19 06 2014) e453.
- [41] P. Maragos, R. Schafer, Morphological skeleton representation and coding of binary images, in: *IEEE Transactions on Acoustics, Speech, and Signal Processing*, 1986, pp. 1228–1244, 34 (5).
- [42] E.R. Dougherty, R.A. Lotufo, *Hands-on Morphological Image Processing*, Bellingham, Wash, SPIE, 2003.
- [43] T.Y. Zhang, C.Y. Suen, A fast parallel algorithm for thinning digital patterns, *Assoc. Comput. Mach.* 27 (3) (01 03 1984) 236–239.
- [44] W. Deng, S. S. Iyengar N. E. Brener, A fast parallel thinning algorithm for the binary image skeletonization, *Int. J. High Perform. Comput. Appl.* 14 (1), pp. 65–81, 01 02 2000.
- [45] K. Donath, M. Wolf, R. Chástek, H. Niemann, A hybrid distance map based and morphologic thinning algorithm, in: *Lecture Notes in Computer Science vol 2781*, Springer, Berlin, Heidelberg, 2003. B. Michaelis und G. Krell, Hrsg.
- [46] B. Efron, Bootstrap methods: another look at the Jackknife, *Ann. Stat.* 7 (1) (01 1979) 1–26.